Group 4

Quantitative Assessment of Metal Artifact Reduction in C-Arm Cone-Beam CT Guidance of Neurovascular Interventions

Carolina Cay-Martínez, Marta Wells
in collaboration with: Jeffrey Siewerdsen, PhD, Tina Ehtiati, PhD and Marty Radvany, MD

Abstract

Purpose: CT guidance of neurovascular interventions is hindered by the presence of streak artifacts caused by metal implants. The purpose of this study is to evaluate the performance of a metal artifact reduction (MAR) algorithm in C-arm cone-beam CT guidance of endovascular treatments for intracranial aneurysms.

Methods: Preclinical studies were conducted using a hollow head phantom with a natural skull in tissue-equivalent plastic. Three clinical procedures were emulated. The intracranial space was successfully filled with combinations of the following materials: brain-equivalent gelatin; plastics representing low-contrast brain; a 3D prototype vascular tree with a PCOM aneurysm (~9 mm diameter); a 3D prototype vascular tree with a Ophthalmic aneurysm (~15 mm diameter); steel, titanium, and tungsten spheres (3.2, 6.4, and 12.8 mm diameter); intravascular stent and coils; and intravascular stent and a liquid embolic system (ONYX) –the last two imaged with and without iodine contrast in the vascular tree. 3D images were acquired using a robotic C-arm (Artis Zeego; Siemens AG) and were reconstructed with and without a MAR algorithm prototype developed by the manufacturer. The MAR algorithm involves semi-automatic segmentation of metal components, sinogram correction, and 3D image reconstruction. Quantifiable parameters were obtained, including artifact magnitude defined as the voxel value standard deviation from streaks in a region about the metal component.

Results: The MAR algorithm demonstrated strong reduction in artifact in each scenario and restored image quality to a level sufficient for visualization of the metal component and surrounding structures. The data show that artifact magnitude is directly proportional to metal density and to the size of the metal implant and that the MAR algorithm segmentation slightly overestimates the volume of the metal component. Nevertheless, the MAR restored accurate visualization of the metal component and did not visibly degrade the fidelity of surrounding structures.

Conclusion: The MAR algorithm provided excellent reduction of artifact magnitude even under challenging scenarios of large and irregularly shaped metal components; however the MAR algorithm also resulted in a slight distortion of the segmented shape of the metal inserts. This quantitative performance assessment indicates that the method warrants investigation in clinical studies. Ongoing work includes streamlining the semi-automatic segmentation step and analysis of tolerance to MAR parameters.

Table of Contents

1. Introduction

Artifacts arising from stents, coils and liquid metal emboli currently present challenges in C-Arm Cone-Beam CT (CBCT) guidance of neurovascular interventions. Metal artifact removal algorithms (MAR) that diminish such artifacts for improved guidance and verification have been recently developed. The objective of this project is to evaluate the performance of such algorithms and identify algorithm components that require further improvement. In order to do so, preclinical studies involving an anthropomorphic head phantom emulating three endovascular interventions for the treatment of intracranial aneurysms were conducted using a robotic C-Arm (Zeego, Siemens Healthcare) for 3D CT imaging.

1.1 Clinical Background

Both ruptured and unruptured aneurysms are typically located in the anastomotic system of arteries that sits at the base of the brain, known as the Circle of Willis. The most common sites for unruptured aneurysms (in order) are: the middle cerebral artery (MCA), posterior communicating artery (PCOM), anterior communicating artery (ACoA), and cavernous internal carotid artery (ICA). The mean diameter of ruptured aneurysms is ~10 mm, while the mean diameter of unruptured aneurysms is ~8 mm. Aneurysm sizes range from less than 3 mm to greater than 25 mm.[1]

Endovascular treatments for intracranial aneurysms include: stent-assisted endovascular coiling, microsurgical clipping and endovascular embolization. Coils used in endovascular coiling procedures are typically made of flexible platinum (stainless steel coils are also available, but less common) and are shaped like thin springs. The coil conforms to the aneurysm shape and seals off the opening of the aneurysm; depending on the size of the aneurysm, more than one coil may be needed to completely separate the aneurysm from the vasculature. About 33-37% of the spherical volume the coil forms when inside the aneurysm is metal.

Stents used in stent-assisted coil embolization are self-expanding stents made typically of nitinol; a nickel and titanium metal alloy. During a stent-assisted embolization, a thin wire (embolic coil) is threaded through a catheter into the affected area in order to fill the weakened portion of the vessel. Due to anatomic features, including wide necks and the incorporation of important branches, endovascular coiling using stent assisted embolization is often a more successful method of treatment.

Clips used in microsurgical clipping are typically made of titanium. Aneurysm clipping consists of isolating the aneurysm from normal blood circulation without blocking any of the small perforating arteries nearby. It is an invasive procedure; a craniotomy and retraction of brain matter is needed to locate the aneurysm and place the clip across the base, or neck. The blades of the clip remain permanently closed on the neck of the artery.

Finally, non-adhesive liquid embolic agents are used for the endovascular embolization of intracranial aneurysms. The material is an ethylene vinyl alcohol copolymer dissolved in the organic solvent dimethyl sulfoxide (DMSO), opacified with tantalum powder. Once it comes into contact with an ionic solution, the DMSO dissipates and the material solidifies into a spongy, cohesive material.
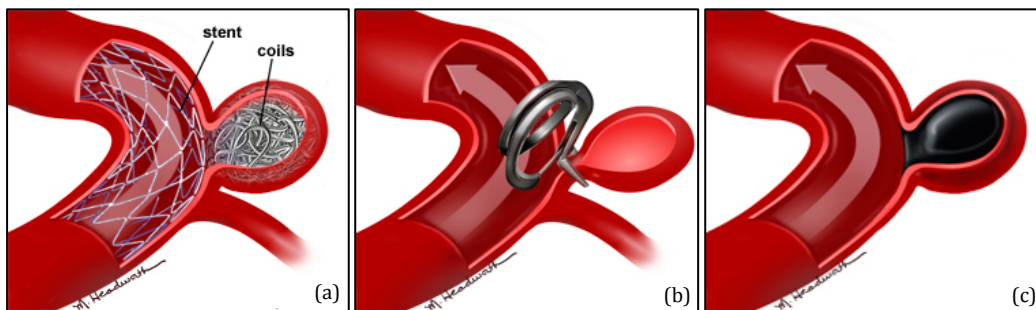

Figure 1. Interventional radiology procedures for treatment of aneurysms: (a) stent-assisted coiling, (b) clipping, and (c) liquid embolization. Images by M. Headworth.

---

[1] **WEIR, Bryce, M.D., et. al.,** "Sizes of ruptured and unruptured aneurysms in relation to their sites and the ages of patients" Journal of Neurosurgery, 96 (2002): 64-70. Print.

1.2 Technical Background

The primary purpose of medical imaging systems is to create accurate reconstructions of the internal structure and function of the body for diagnostic purposes or interventional treatment of diseases. The ability of medical professionals to successfully accomplish these tasks strongly depends on the fidelity of the images (the degree to which the image successfully represents the anatomy) and the quality of the images (the degree of distortion introduced into the image). Metal objects present in a CT image introduce metal artifacts that are caused by beam hardening (a shift in detected mean energy), photon starvation (insufficient photons reach the detector), partial volume effects (off-centered dense objects partway into the width of the beam), and undersampling. These artifacts result in heavy streaking patterns that emanate radially from the metal object and hinder accurate visualization of the image.

The metal artifact removal algorithm used in the MAR application is an InSpace DynaCT MAR-prototype software made available by Siemens Healthcare and based on work by Prell, et. al. The approach follows a quasi-iterative, three-step correction scheme that uses a forward projection-based calculation of surrogate attenuation values per detector element for each projection with a dedicated segmentation process of the initial corrected image. The system algorithm steps, show in Figure 1, are as follows:

1. The system performs a standard reconstruction.
2. The user is prompted to window and crop a volume containing only the metal implant. The region must be selected to avoid situations where the maximum gray value of the selected region is smaller than the default minimum metal threshold. A three-dimensional segmentation using a thresholding operation of the metal implant is performed.
3. The first correction uses a three-dimensional interpolation scheme and is followed by a second reconstruction to obtain a metal artifact reduced *transition volume*.
4. The second correction performs a clustering of the *transition volume* followed by a forward projection of the tissue-class model onto each metal affected detector element. Subsequently a final reconstruction is performed to obtain the *corrected volume*.
5. A final optimization step reduces, or removes, residual streaks from the *corrected volume*.
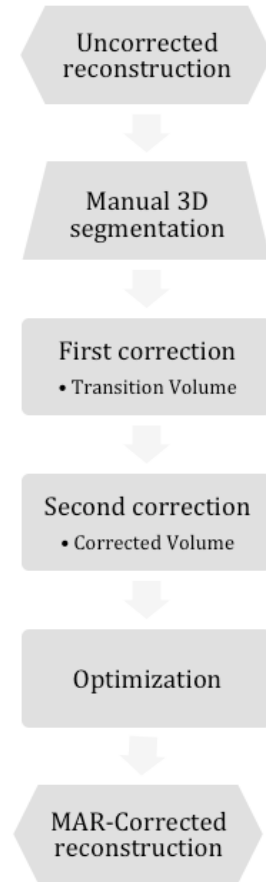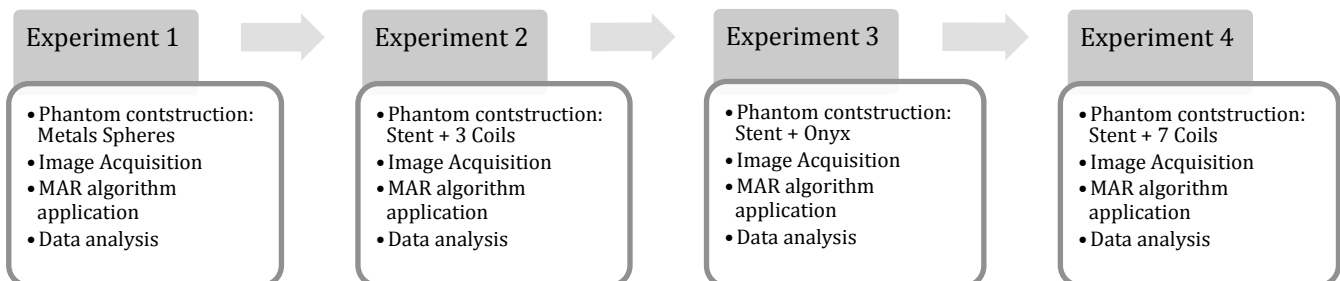

Figure 1. Flow chart of the DynaCT MAR–prototype algorithm steps.

2. Technical Approach

The project was divided into four experimental stages. Each stage consisted of the following chronological steps: construction of the phantom, CT image acquisition, application of the MAR algorithm on the acquired data, and quantitative data analysis. Figure 2 shows the project approach.
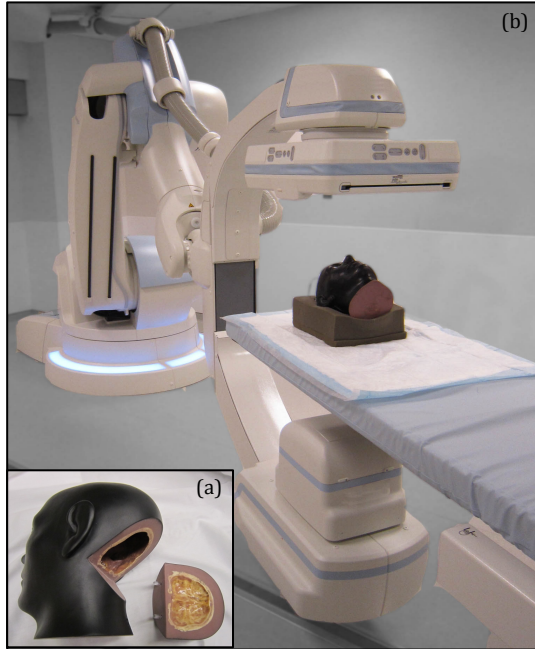

4

The hollow anthropomorphic head phantom used for the simulation of the endovascular intervention procedures consisted of a natural human skeleton in tissue-equivalent plastic (The Phantom Laboratory, Greenwich, NY). An opening at the posterior base of the skull allowed the intracranial space to be filled with brain-equivalent gelatin, relevant soft-tissue simulating plastics, prototype vasculature and metal components. All scans were performed on a C-arm cone-beam Axiom Artis Zee (Axiom Artis Zeego, Siemens Medical Solutions, Elangen, Germany) with a flat panel detector. Standard DynaCT head acquisition were obtained involving the parameters shown below:

Parameter	Value
Tube voltage	70 kV
Tube current	235 mA
Rotation time	20 s
Angle increments	0.4°
Number of frames	496
Frame rate	30 frames/s
Degrees in orbit	198.4°

Figure 3. Experimental setup; (a) hollow head phantom and (b) Siemens C-arm cone-beam CT. Image provided by I-star lab.

Post-acquisition processing of CT image data was performed on the dedicated Leonardo workstation (syngo, Siemens) using the syngo InSpace3D reconstruction algorithms. File formats for raw data (including relevant calibration files), reconstructed data and MAR corrected data were successfully obtained for each phantom. The metal artifact removal algorithm used in the MAR application is an InSpace DynaCT MAR-prototype software made available by Siemens Healthcare.

Data analysis for the images acquired during the preclinical studies comprises of both image quality and image fidelity assessments. Image quality assessments include the measurements of contrast, noise and artifact magnitude whereas image fidelity assessments include the accuracy of the metal segmentation and the accurate anatomical reproduction of metal implants and surrounding soft tissues. Mathematical manipulations of the raw data and acquired images were performed in MATLAB.

2.1 Phantom Construction and Image Acquisition

2.1.1 Model I: Metals Spheres

The phantom constructed during the first stage of the project incorporated metal spheres of different diameters and attenuation properties, as well as various plastic spheres to simulate low-contrast brain tissues. Metal spheres were the simplest materials available to simulate both the shape and sizes of aneurysms densely packed with coils and the composition of the various metallic objects used in different endovascular interventional procedures. Additionally from the metal components, the following twelve plastic spheres of six different materials were inserted in the brain-equivalent gelatin: two of polypropylene, two of low-density polyethylene, two of high-density polyethylene, two of acrylic, two of nylon, and two of acetal. Their exact placement within the phantom was not critical; their primary function was to measure the HU units of the plastic materials and determine which relevant soft tissue (CSF, white or grey matter, etc.) they approximated.

5

Material	HU units (approximations)	Simulated neurovascular tissue
Polypropylene	-100	Fat
Low-density polyethylene	+10	CSF
Gelatin	+40	Grey/white matter
High-density polyethylene	+40	Grey/white matter
Acrylic	+100	High-contrast agent
Nylon	> 100	High-contrast agent
Acetal	> 100	High-contrast agent

Table 1. Materials of plastic spheres and relevant information

In order to accurately simulate the clinical procedures of intracranial aneurysm coiling, clipping and embolization, three diameters and three materials of metal spheres were used: 3.2 mm, 6.4 mm, and 12.7 mm each of titanium, steel and tungsten. More specifically, nine metal spheres total were used in the imaging phantom: three titanium grade 5 spheres of diameter 3.2 mm, 6.4 mm and 12.7 mm each, three 316 resistant stainless steel spheres of diameter 3.2 mm, 6.4 mm and 12.7 mm each, and three tungsten carbide spheres of diameter 3.2 mm, 6.4 mm and 12.7 mm each. Note that tungsten, atomic number Z = 74, is used as a substitute for platinum, atomic number Z = 78, due to their similar attenuation properties. All metal spheres were acquired from McMaster-Carr®.

Material of metal spheres	Simulated metal object
Titanium	Titanium clips / nitinol stents
316 Stainless Steel	Steel coils
Tungsten Carbide	Platinum coils

Table 2. Material of metal spheres and relevant information

2.1.2 Model II: Stent-Assisted Endovascular Coiling

The second and fourth experimental stage of the project consisted of the construction of phantoms that incorporated an aneurysm vessel model, plastic spheres with appropriate contrast to approximate the simulation of blood clots, plastic rods to simulate non-contrast enhanced blood, surgical coils and stents. The various acquisitions included the use of a non-enhanced saline solution and a contrast-enhanced iodine solution. All model materials simulated the relevant soft-tissues and instruments found in an interventional angiographic stent-assisted endovascular coiling procedure.

A preliminary vasculature vessel model was developed from 6.4 mm diameter vinyl plastic tubing and heat-shrinkable plastic. A 3.2 mm plastic sphere and the concentrated application of heat were used to mold an aneurysm shape in the shrinkable plastic material. The preliminary model, shown in Figure 4.a, was not used in any experiment.

Two 3D vascular tree aneurysm vessel models were acquired from Vascular Simulations: the first vessel tree modeled a PCOM aneurysm with an ~8 mm diameter (used in the second stage of the project), and the second vessel tree modeled an ophthalmic aneurysm with a ~15 mm diameter (used in the fourth stage of the project). Four
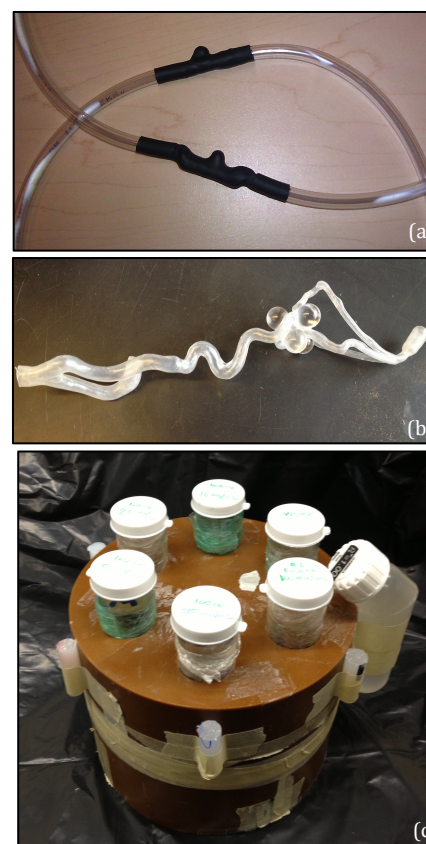

Figure 4. Experimental setup: (a) developed vessel model, (b) vessel tree from Vascular Simulations, and (c) iodine contrast phantom. Images provided by

6

high-density acrylic plastic spheres were placed adjacent to both aneurysm vessel models to simulate blood clots. The vessel model used in the second stage phantom is shown in Figure 4.b. Six polypropylene rods were also placed in the surrounding brain-equivalent gelatin to simulate non-contrast enhanced blood.

Iodine contrast and x-ray angiography is used in stent-assisted endovascular coiling to quantify blood flow and to map the vessel anatomy. In clinical cases, the cardiovascular system filters and dilutes the iodine before it reaches the cerebral arterial circle. In the presented phantom model, an ideal concentration of iodine (30 mgI/mL) was found such that it would produce a contrast attenuation of about 1100-1200 HU without dilution through circulation in the body. In order to find the correct iodine dilution, a phantom was created that contained: six solutions of different iodine contrast agent (Omnipaque) concentrations (100, 75, 50, 20, 10, and 0 mgI/mL) placed in a simple cylinder phantom along with seven unidentified plastic rods. Linear interpolation was used to find the ideal dilution.
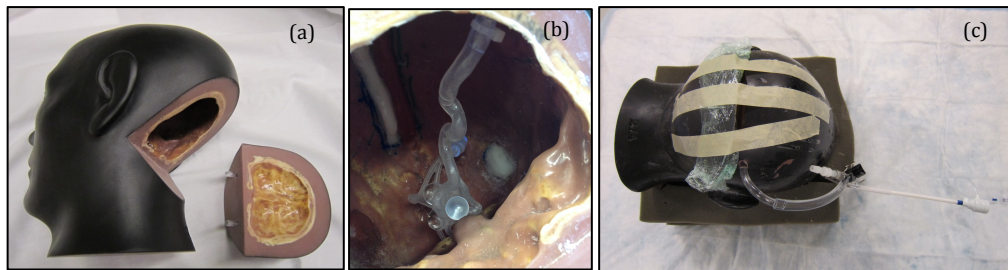

Figure 5. Experimental setup: (a) hollow head phantom with opening (b) vessel tree with high-density acrylic plastic spheres placed inside hollow head phantom and (c) phantom placed in prone position with sheath attached to superior-anterior hole. Images provided by the I-star lab and Cay and Wells.

2.1.3 Model III: Liquid Embolization

The phantom constructed during the third stage of the project incorporated the first aneurysm vessel tree (PCOM aneurysm with an $\sim$ 8 mm diameter shown in Figure 4.b), acrylic spheres with appropriate contrast to approximate the simulation of blood clots, polypropylene rods to simulate non-contrast enhanced blood, a stent and the Onyx Liquid Embolic System. The Onyx Liquid Embolic System (LES, Covidien) is composed of ethylene vinyl alcohol copolymer dissolved in the organic solvent dimethyl sulfoxide (DMSO) opacified with tantalum powder. A 1.5 ml vial of Onyx 34 (8% EVOH) and a 1.5 ml vial of DMSO were used in the procedure. The various acquisitions included the use of a non-enhanced saline solution and a contrast-enhanced iodine solution. All model materials approximately simulated the relevant soft-tissues and instruments found in interventional aneurysm embolization as well as pre-surgical embolization of brain arteriovenous malformations (AVM) procedures.

2.1.4 Image Acquisition Procedures

Model I: the plastic spheres were introduced into the semi-hardened brain-equivalent gelatin prior to the image acquisition. During image acquisition, the metal spheres were sequentially inserted and removed from the intracranial cavity. For easy insertion and removal, each metal spheres was attached to a plastic rod and lubricated with water, so as to not introduce air into the brain gelatin. Each metal sphere was placed as close to the clivus and sella as possible in order to approximate the location of real-world scenarios of common intracranial aneurysms. Careful consideration of the positions of the plastic spheres was taken so as to not alter their position throughout the image acquisition procedure. For further information, please refer to appendix A1.

Model II: two 6.35mm diameter holes were drilled in the anthropomorphic phantom skull prior to the image acquisition procedure. One hole was positioned superior-anterior, the other inferior-posterior to the cerebral skull; locations were chosen for their vessel accessibility advantages. The vasculature tree aneurysm model used in the specific project stage was placed such that the superior opening exited the superior-anterior hole, while the inferior opening exited the inferior-posterior hole. The six polypropylene plastic rods were then placed in the semi-hardened gelatin surrounding the vasculature tree (careful consideration was taken so as to not introduce air). A 30mgI/mL iodine solution was prepared for contrast-

enhanced procedures. During image acquisition, the surgeon performed a standard clinical stent-assisted endovascular coiling procedure: a thin guide wire was threaded through a catheter into the affected area of the brain and a stent was deployed in the aneurysm neck to support the weakened portion of the vessel. A catheter was later inserted through the stent and into the aneurysm space in order to deploy the coils. For further information on both the second stage and fourth stage phantom image acquisitions, please refer to appendices A2 and A4, respectively.

Model III: techniques performed pre-acquisition follow the same steps as described previously. During image acquisition, the surgeon performed a standard clinical liquid embolization: a thin guide wire was threaded through a catheter into the affected area of the brain and a stent was deployed in the aneurysm neck to support the weakened portion of the vessel. An occlusion balloon catheter was inserted in order to deploy a hyper-form single lumen balloon. Note that this step was not successful, but it did not hinder further progress in the procedure. A catheter was later inserted through the stent and into the aneurysm space in order to deploy the coils. A DMSO compatible catheter was then inserted through the stent and into the aneurysm space in order to introduce a solution of Onyx 34 MTI. For further information of the third stage phantom image acquisition, please refer to appendix A3.

2.2 MAR Application

The MAR-prototype algorithm was successfully applied to all acquired CT data. Nevertheless, we encountered problems in the initial MAR application on the first experimental stage data due to a C-arm calibration error that resulted in the introduction of geometric calibration artifacts into the images (see Figure 6). After C-arm calibration, a new calibration file was obtained and images were reconstructed again. Geometric calibration artifacts were corrected with the acquisition of the new files. Additional licensing, algorithmic and prototype accessibility difficulties hindered further application of the MAR prototype. For more information, please refer to the project management section. MAR application technique for the first experimental stage phantom was run under the assumption that there was data truncation present in the edges of the phantom image, due to the fact that some of the edges of the phantom lay outside of the field of view. MAR application for the other experimental stages were run with the standard procedure for no data truncation.
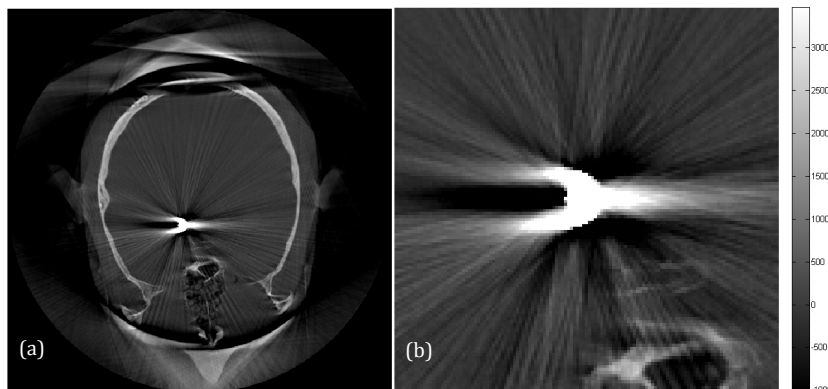
Figure 6.
(a) Image of 6.4 mm steel sphere. (b) Zoomed in portion of sphere. Notice the annular shape of the emanating streaks is a geometric artifact.

2.3 Data Analysis

For every data set, z-axis transverse slices of the acquired images were analyzed. Regions of interest (ROIs) were selected both in regions inside the metal component and in regions directly surrounding the metal component, but excluding the component itself. Background ROIs were chosen so that they only encapsulated brain-equivalent gelatin and no other simulated soft tissue, vasculature or bone. For selected sets of images, ROIs were placed in plastic spheres that had been inserted in the surrounding brain-equivalent gelatin. ROI selection is shown in the images found in the results section. For further information on ROI selection and algorithm, please refer to appendix B.

The objective of the data analysis was to quantitatively measure and assess both image quality and image fidelity. Table 3 shows the measurements and equations used for such analysis. Basic measurements of mean and standard deviation of HU values were calculated both in component ROIs and background ROIs. Image quality assessments include the measurements of contrast, noise and *artifact magnitude*, defined as the average standard deviation in the background ROIs. Image fidelity assessments include the accuracy of the metal segmentation (measured by volume, surface area and sphericity) applied to the metal spheres and the accuracy of the contrast of surrounding plastic spheres/rods. All calculations were made voxel-wise. For more detailed algorithmic and mathematical information, please refer to appendix B.

Measurement	Unit	Description	Symbol/Equation
Mean	HU		$\mu_{component}$ & $\mu_{background}$
Artifact magnitude	HU	Defined as the standard deviation of the background ROI	$\sigma_{background}$
CNR		Contrast-to-noise ratio	$\dfrac{\mu_{component} - \mu_{background}}{\sigma_{background}}$
CT number error	%	A value of zero indicates perfect reproduction of control CT numbers	$\left\lvert \dfrac{\mu_c^{true} - \mu_c^{measured}}{\mu_c^{true}} \right\rvert \cdot 100$
Volume	mm^3		V_c
Surface area	mm^2		A_c
Volume accuracy	%	A value of 100 is a perfect reproduction of true volume	$\left\lvert \dfrac{V_c^{measured}}{V_c^{true}} \right\rvert \cdot 100$
Surface area accuracy	%	A value of 100 is a perfect reproduction of true surface area	$\left\lvert \dfrac{A_c^{measured}}{A_c^{true}} \right\rvert \cdot 100$
Sphericity		A value of 1 describes a perfectly spherical object	$\psi = \dfrac{\pi^{1/3}(6V_c)^{2/3}}{A_c}$

Table 3. Quantitative metrics for data analysis

3. Results and Discussion

3.1 Model I: Metal Spheres

Uncorrected and MAR corrected images of the various metal spheres are shown in Figure 8. Basic measurements of mean HU values of both metal sphere component ROIs and background ROIs are shown in Table 4. The average HU value in the uncorrected images of metal component ROIs among the different diameters of titanium was ~11,000 HU; steel was ~20,000 HU; and tungsten was ~21,000 HU. This finding supports the hypothesis that higher density metals will have higher attenuation coefficients, and therefore higher HU values than lower density metals. The average HU value of regions spaced across the brain-equivalent gelatin among all images is ~40 HU, which demonstrates an accurate simulation of cerebral grey matter.
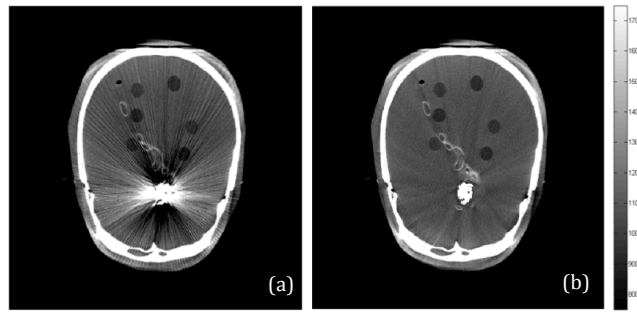
Figure 7. Full view of brain phantom CT image for the fourth experimental stage. (a) uncorrected and (b) MAR corrected.

Metal	Diameter	μ_{sphere} (HU)		$\mu_{background}$ (HU)		Artifact magnitude (HU)	
		UC	MAR -C	UC	MAR -C	UC	MAR-C
Titanium	Small	11,580 ± 1,500	12,560 ± 5,000	-29 ± 1	-22 ± 1	94 ± 7	50 ± 4
	Medium	12,650 ± 500	13,680 ± 500	-1 ± 2	-4 ± 4	228 ± 36	47 ± 4
	Large	8,490 ± 800	9,520 ± 800	-8 ± 8	-17 ± 7	299 ± 39	60 ± 13
Steel	Small	27,020 ± 1,900	27,420 ± 1,800	-2 ± 5	-3 ± 1	314 ± 67	47 ± 2
	Medium	23,100 ± 900	24,970 ± 900	-5 ± 10	-13 ± 2	461 ± 54	43 ± 1
	Large	8,980 ± 1,900	10,080 ± 1,900	11 ± 4	-12 ± 10	405 ± 24	48 ± 3
Tungsten	Small	28,430 ± 1,400	28,600 ± 1,400	19 ± 8	14 ± 2	440 ± 76	48 ± 4
	Medium	23,890 ± 1,800	24,730 ± 1,700	-8 ± 12	-28 ± 9	472 ± 33	45 ± 1
	Large	9,810 ± 2,100	10,920 ± 2,100	51 ± 13	86 ± 6	568 ± 13	43 ± 3

Table 4. Mean HU values of metal component and background ROIs for the nine spheres, and artifact magnitude values for the nine spheres of small (3.2mm), medium (6.4) and large (12.8 mm) diameters.
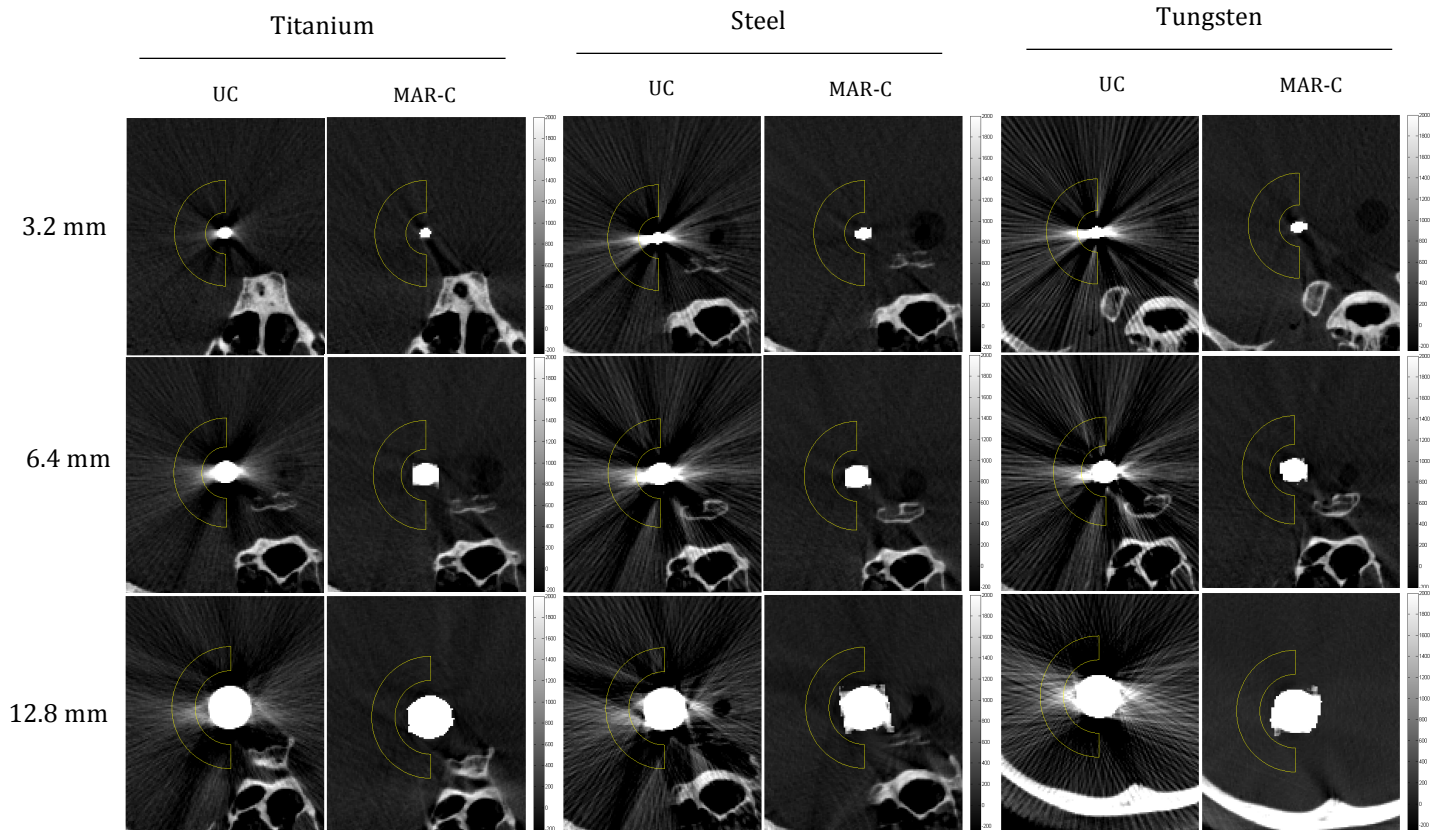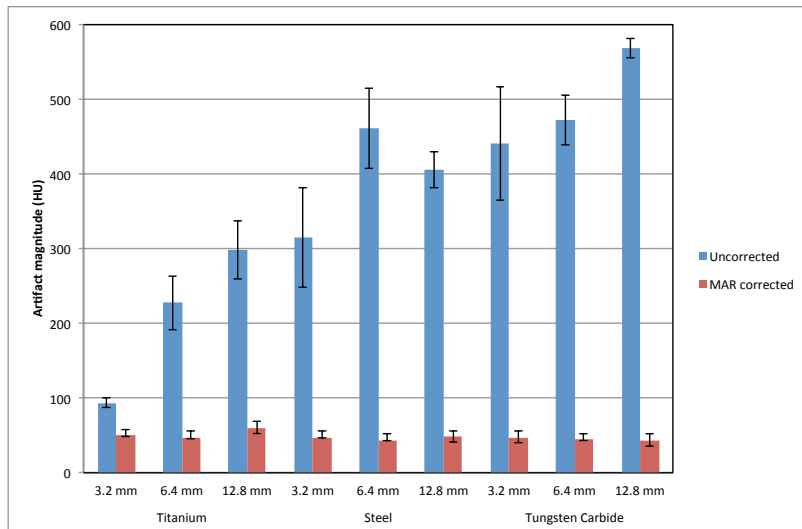

Figure 8. Images of the nine spheres. Columns show uncorrected (UC) and MAR corrected (MAR-C) images of titanium, steel, and tungsten carbide spheres. Rows show different diameters of the spheres. Background ROI are shown in yellow.

10

Graph 1.
Artifact magnitude of uncorrected and MAR corrected CT data of varying metal spheres. Notice that artifact magnitude in uncorrected data is directly proportional to the density and diameter of the metal sphere. Also notice the MAR algorithm corrects the artifact to a constant level, regardless of density or diameter.

As previously described, metal artifacts cause streaks to emanate from metal implants. The background ROIs were selected to contain a sufficient amount of the streaking patterns in order to measure their *artifact magnitude* difference between the uncorrected and corrected data. The data show that artifact magnitude is directly proportional to metal density and to the size of the metal implant. As the density and size of the material increases, so does the artifact magnitude: this is due to beam hardening effects (the denser material will attenuate a larger amount of lower energy photons). The MAR corrected data shows a significant decrease in artifact magnitude across all metal sphere densities and diameters. The average resulting artifact magnitude across all metal spheres was 48 ± 4, which implies a consistent correction regardless of material density or size. This effect is shown in Graph 1.

In theory, the MAR algorithm should segment and produce reconstructed spheres that are an accurate, if not an identical, representation of the original spheres. In order to test this hypothesis, the volume of the spheres and their sphericity were measured in both the MAR reconstructed images and uncorrected images. Table 5 shows the calculated volume, surface area and sphericity of the various spheres. On average, values for volume and surface area are higher for the MAR corrected images. At a statistical significance level of $\alpha=0.1$, volume and surface area in the uncorrected and MAR corrected data sets are significantly different with p-value for volume of 0.034 and for surface area of 0.089. Thus, we can conclude that the MAR segmentation overestimates the volume and, to a lesser degree, the surface area of a component's shape. Values for sphericity are not significantly different between the uncorrected and MAR corrected data sets, with a p-value of 0.48. Therefore, the MAR algorithm volume overestimation is equally distributed over the entire metal component without distorting the shape.

Volume and surface area accuracy values, shown in Table 6, are larger thatn 100%, which implies that both uncorrected and MAR corrected data overestimate the true volume and surface area values of the known spheres. The values in the MAR segmentation are also higher for larger spheres. This is due to the fact that the accuracy is proportional to the size of the voxel; for smaller spheres, the same size voxel will cause a greater distortion effect in segmentation than for larger spheres.

Metal	Diameter	Volume, V_c (mm³)			Surface Area, A_c (mm²)			Sphericity	
		True	UC	MAR-C	True	UC	MAR-C	UC	MAR-C
Titanium	Small	17	20	22	32	54	59	0.665	0.652
	Medium	137	153	162	128	206	215	0.671	0.669
	Large	1098	1155	1195	515	793	812	0.672	0.671
Steel	Small	17	32	34	32	81	79	0.604	0.640
	Medium	137	182	191	128	235	242	0.660	0.662
	Large	1098	1248	1277	515	839	851	0.669	0.669
Tungsten	Small	17	41	39	32	97	86	0.588	0.643
	Medium	137	188	194	128	238	245	0.669	0.663
	Large	1098	1287	1337	515	855	899	0.670	0.653

Table 5. Volume, surface area and sphericity calculations for the nine metal spheres of small (3.2mm), medium (6.4) and large (12.8 mm) diameters.

Metal	Diameter	Volume accuracy (%)		Surface area accuracy (%)	
		UC	MAR-C	UC	MAR-C
Titanium	Small	118	129	168	182
	Medium	111	118	160	167
	Large	105	109	154	158
Steel	Small	186	195	250	244
	Medium	132	139	183	188
	Large	114	116	163	165
Tungsten	Small	236	225	302	267
	Medium	137	141	185	190
	Large	117	122	166	174

Table 6. Volume, and surface area accuracy measurements for the nine metal spheres of small (3.2mm), medium (6.4) and large (12.8 mm) diameters.

C-Arm Cone-Beam CT systems obtain a certain number of projections for a given orbit. The Zeego system used for this project obtained 496 projections in a 198.4° orbit. In order to reconstruct the image, projections are added and later backprojected. The results of all experimental data sets show a particular prominent streak in a lateral orientation, resembling a "bow". This effect is due to the fact that the start and stop positions of the particular orbit used are half-annular, and is responsible for inaccuracies in the measured segmentation of metal component values. Potential areas for improvement in the semi-automatic segmentation step of the MAR algorithm include taking into consideration the orbital pattern in order to make the segmentation sensitive to the start and stop positions of the orbital path.

3.2 Model II: Stent-Assisted Endovascular coiling

Uncorrected and MAR corrected images of the second experimental stage are shown in Figure 9. This stage included three coils alone and with an endovascular stent in the ~8 mm diameter PCOM aneurysm vessel model imaged in both non-contrast and contrast-enhanced solutions. Uncorrected and MAR corrected images of the fourth experimental stage are shown in Figure 10. This stage included a set of a half-coiled (two coils) ~15 mm diameter Ophthalmic aneurysm and a fully-coiled (seven coils) aneurysm, both with an endovascular stent imaged in non-contrast and contrast-enhanced solutions. Table 7 shows that the MAR algorithm application in both experimental stages decreases the artifact magnitude values in the non-contrast and contrast-enhanced vessels.

Metal	Vessel	Artifact magnitude (HU)	
		UC	MAR -C
3 Coils	NC	380 ± 34	33 ± 4
	CE	355 ± 38	38 ± 4
3 Coils + Stent	NC	382 ± 42	39 ± 3
	CE	380 ± 35	46 ± 3
Half-coiled + Stent	NC	316 ± 76	40 ± 2
	CE	329 ± 76	65 ± 12
Fully-coiled + Stent	NC	360 ± 67	37 ± 3
	CE	385 ± 64	41 ± 2

Table 7. Artifact magnitude values for second and fourth experimental stages of stent-assisted endovascular coiling procedures.
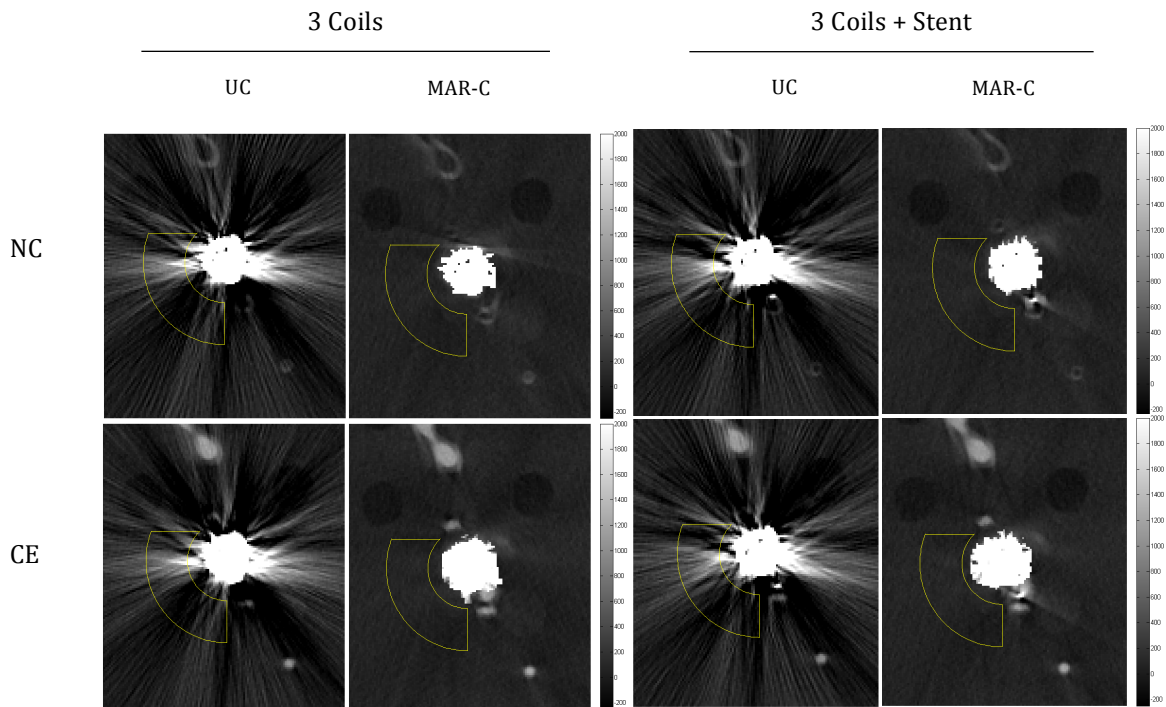
Figure 9. Uncorrected (UC) and MAR corrected (MAR-C) CT images of 3 coils with and without a stent., both with non-enhanced (NC) and contrast-enhanced (CE) solutions. Background ROIs are shown in yellow.
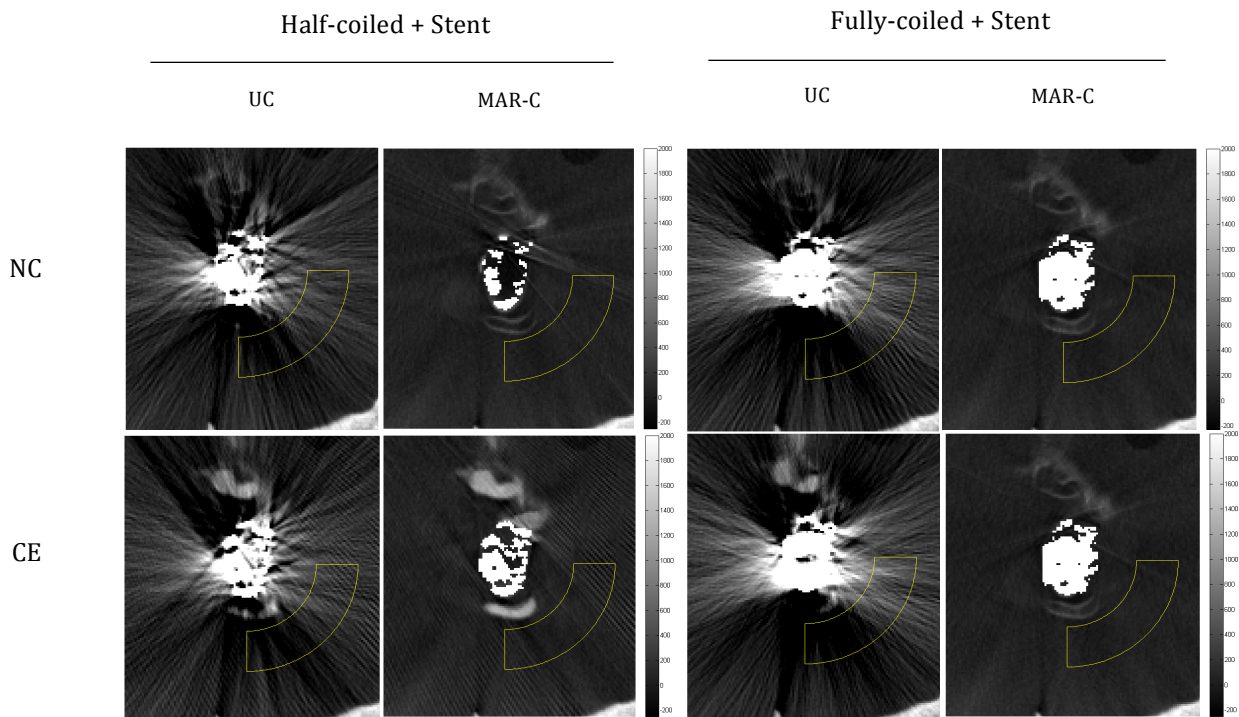
Figure 10. Uncorrected (UC) and MAR corrected (MAR-C) CT images of a half-coiled and fully-coiled aneurysm both with a stent and non-enhanced (NC) and contrast-enhanced (CE) solutions. Background ROIs are shown in yellow.

In order to assess image fidelity of the acrylic spheres and the polypropylene rods, specific background ROIs in close proximity of the plastic inserts and component ROIs contained within the plastic inserts were selected, as shown in Figure 11 (this process is applied to both the second and fourth experimental stages). Contrast is a measure of the magnitude difference of value between a target object and the surrounding background. A contrast-to-noise ratio value of around 2 allows for a fair visual distinction of the target from its background. However, the metal streak completely obscured the plastic inserts. Thus the

placement of plastic component ROIs incorrectly measured the contrast of the metal artifact streaks compared to the background rather than the plastic inserts compared to the background. This led to unnaturally high CNR values for uncorrected data sets inconsistent with qualitative visual inspection.

Therefore, a different quantitative metric was necessary to determine the image fidelity of the plastic inserts. CT number error measures the percent error of the contrast of the plastic inserts as compared to their values in control images. For all data sets, 3 coils with and without a stent and the fully-coiled aneurysm, results show that CT number error greatly decreases for the MAR corrected images.

Figure 11
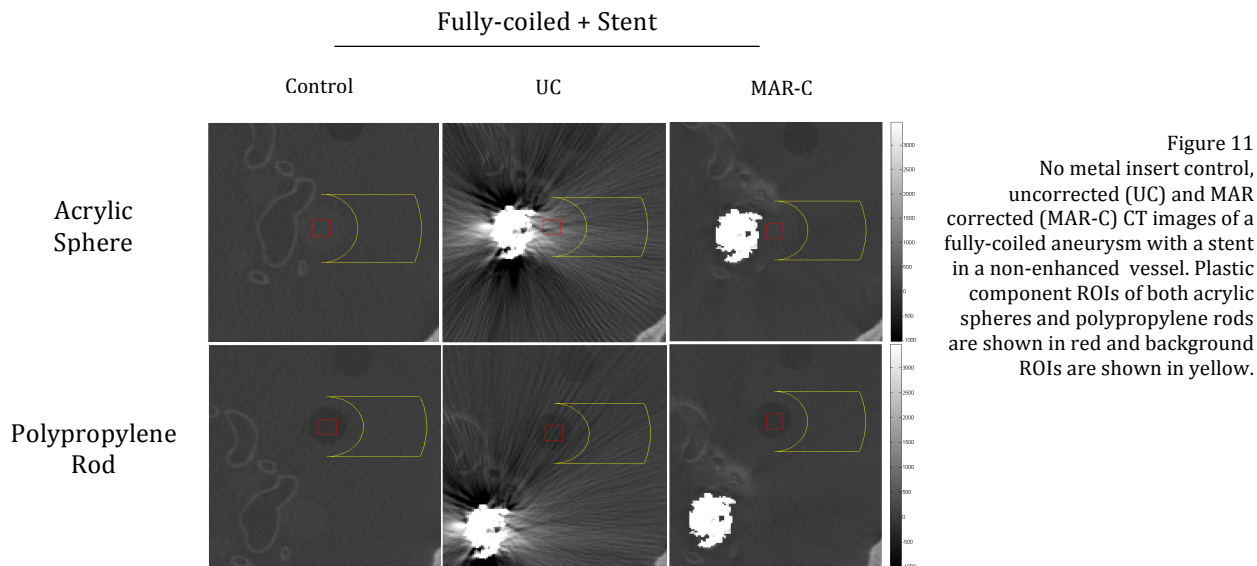No metal insert control, uncorrected (UC) and MAR corrected (MAR-C) CT images of a fully-coiled aneurysm with a stent in a non-enhanced vessel. Plastic component ROIs of both acrylic spheres and polypropylene rods are shown in red and background ROIs are shown in yellow.

Metal	Vessel	CT number error (%)				CNR			
		Acrylic Sphere		Polypropylene Rod		Acrylic Sphere		Polypropylene Rod	
		UC	MAR-C	UC	MAR-C	UC	MAR-C	UC	MAR-C
3 Coils	NC	260	6	133	20	1.9	2.4	3.0	4.5
	CE	293	11	65	53	1.8	1.4	3.6	4.3
3 Coils + Stent	NC	234	6	160	21	2.0	2.6	3.4	4.5
	CE	261	37	76	42	1.9	1.4	3.6	4.9
Fully-coiled + Stent	NC	946	43	102	11	5.2	1.0	2.8	5.1
	CE	757	89	152	11	6.1	0.6	3.0	4.2

Table 8. CT number accuracy and CNR values of acrylic and polypropylene rods in various stent-assisted endovascular coiling models.

3.2 Model III: Liquid Embolization

Uncorrected and MAR corrected images of the third experimental stage are shown in Figure 12. This stage included a liquid embolic system (Onyx) with an endovascular stent in the ~8 mm diameter PCOM aneurysm vessel model imaged in both non-contrast and contrast-enhanced solutions. Table 9 shows that the MAR algorithm application decreases the artifact magnitude values in the non-contrast and contrast-enhanced vessels.

During the procedure for this experimental stage, the hyper-form balloon failed to deploy. As such, the liquid embolus was not fully contained within the aneurysm; some leaked into the adjacent vessel. As seen in Figure 12, the Onyx shape does not conform to the spherical aneurysm and streaks are therefore not as uniformly distributed as in other data sets. Due to this pitfall, manual segmentation of the metal component was limited to the largest portion of the Onyx, leaving smaller separate pieces un-segmented. This lead to a slightly deviated MAR correction of the data, therefore, although artifact magnitude is decreased, it is decreased at a lower ratio; the Onyx artifact magnitude values of uncorrected data were, on average, 3.5

times higher than MAR corrected data. In parallel, the coiling model artifact magnitude values of uncorrected data were, on average, 8.4 times higher than MAR corrected data. These results are visually presented in Graph 2.

CNR and CT number errors are shown in Table 10. Again, CNR are inconsistent with qualitative visual inspection due to obscuring streak patterns. CT number errors are not an accurate reflection of the true image fidelity due to the abovementioned pitfalls.
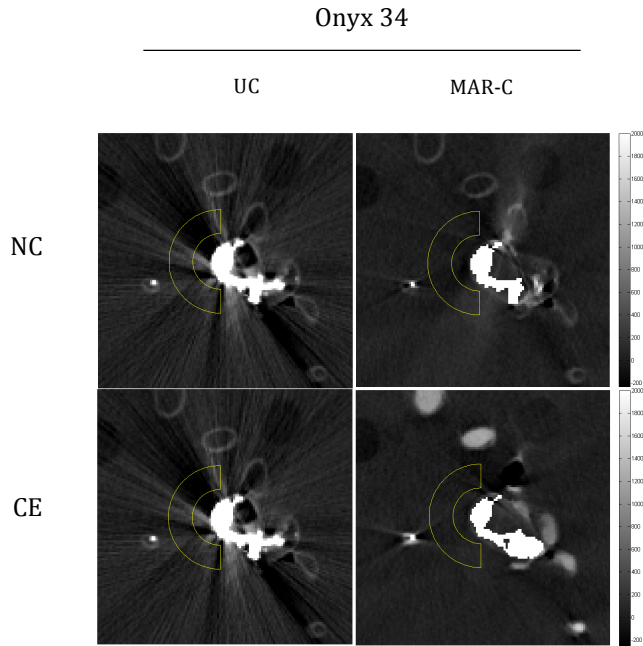
Metal	Vessel	Artifact magnitude (HU)	
		UC	MAR -C
Onyx 34	NC	302 ± 77	72 ± 15
	CE	248 ± 61	91± 15

Table 9. Artifact magnitude values for liquid embolus in non-enhanced (NC) and contrast enhanced (CE) vessels.

Figure 12.Uncorrected (UC) and MAR corrected (MAR-C) CT images of a liquid embolus in non-enhanced (NC) and contrast-enhanced (CE) solutions. Background ROIs are shown in yellow.

Metal	Vessel	CT number error (%)				CNR			
		Acrylic Sphere		Polypropylene Rod		Acrylic Sphere		Polypropylene Rod	
		UC	MAR-C	UC	MAR-C	UC	MAR-C	UC	MAR-C
Onyx	NC	33	55	43	97	0.5	3.5	1.2	1.4
	CE	13	2	51	95	1.0	1.8	2.6	1.2

Table 10. CT number accuracy and CNR values of acrylic and polypropylene rods in liquid emulous model.
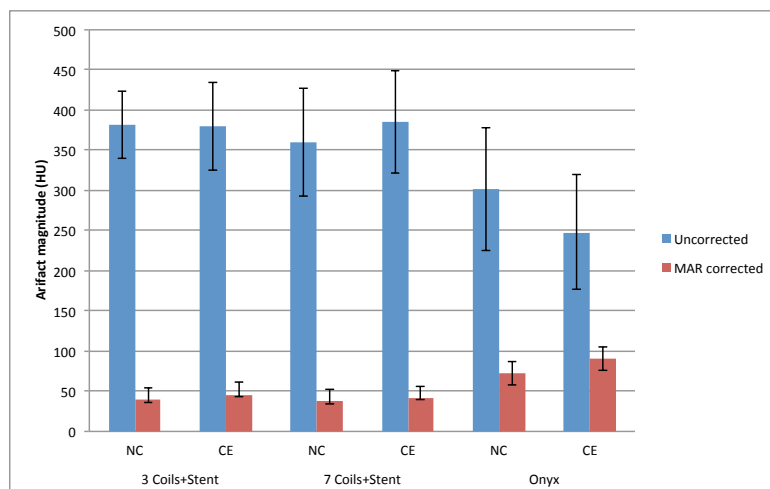
4. Conclusion

The MAR algorithm provided excellent reduction of artifact magnitude even under challenging scenarios of large and irregularly shaped metal components as shown in data sets of all modeled neurovascular interventions. However, volume and surface area accuracy calculations demonstrate that the MAR algorithm also resulted in a slight overestimation of the reproduced segmented shape of the metal spheres.

Quantifiable assessments of image quality and image fidelity are usually difficult to measure without an inherent amount of subjectivity. Standard procedures to evaluate the reduction in quality caused by metal artifacts are based on subjective perceptions of image distortion. Although our measurements did include the use of manual placement of regions of interest (ROIs) based on visual interpretations of the images, the metrics we developed for quantifying artifact magnitude and visualization of structures rely solely on quantifiable data rather than qualitative assessments. This quantitative performance assessment indicates that the MAR method warrants investigation in clinical studies: quantifying image quality is critical for the evaluation of new imaging technologies and algorithms, providing evidence for translation to clinical use, and avoiding the pitfalls of subjective interpretation.

We suggest that the segmentation step of the MAR algorithm should be streamlined and analysis of tolerance to MAR threshold parameters should be examined. The manual segmentation step in the MAR algorithm relies heavily on precise user input, which likely leads to unnecessary deviations in MAR efficacy. Therefore, we recommend more automation of this step in particular as the most prevalent issue. Additionally, we found the MAR software to be less than user-friendly; the system crashed more so in times when we deviated from the SOP, specifically when manually segmented region did not contain any metal.

Future work includes streamlining the semi-automatic segmentation step, comparison to other MAR methods (eg. Known-Component Reconstruction [Stayman, et. al.]), and segmentation approaches to find an optimal combination of MAR algorithm steps. MAR algorithms are shown to improve visualization and are ready for clinical-based trials.

5. Project Management

The project was comprised of four experimental stages, each stage included a phantom model construction, a C-Arm Cone-Beam image acquisition, a MAR application, and data analysis of uncorrected and MAR corrected data. Shown in table XXX are the project milestones and their dates of completion.

MAR project milestones	Date
Project selection	2/09
Clinical and technical background research	2/10-2/16
First stage phantom construction	2/21
Image acquisition of first phantom in Zeego (C-arm Cone-Beam CT)	2/28
Calibration of Zeego (C-arm Cone-Beam CT)	3/19
Reconstruction and application of MAR algorithm to first phantom images	3/20
Iodine phantom construction	3/21
Image acquisition of iodine phantom in Zeego	3/29
Image acquisition of second phantom in Zeego	4/05
Reconstruction and application of MAR algorithm to second phantom images	4/08
Third stage phantom construction	4/16, 4/18
Image acquisition of third phantom in Zeego	4/19
Fourth stage phantom construction	4/29
Image acquisition of fourth phantom in Zeego	5/03

5.1 Accomplished vs Planned

Original plan:

Phantom construction:
- Min: metal spheres
- Exp: coils and/or clips
- Max: liquid embolus

Image Acquisition:
- Min : experimental bench in I-star lab
- Exp : Zeego
- Max : algorithm for data conversion between Zeego and bench

Data Analysis:
- Min: CNR, application of MAR on data
- Exp: artifact magnitude and quantitative parameters for segmentation accuracy
- Max: other quantitative image quality metrics and segmentation algorithm improvement suggestions

MAR algorithm:
- Min: application of MAR on data
- Exp: metrics to measure accuracy
- Max: algorithm improvements

Accomplished Plan:

Phantom construction:
- Min: metal spheres
- Exp: coils and stent
- Max: liquid embolus

Image Acquisition:
- Min : none
- Exp : Zeego
- Max : none

Data Analysis:
- Min: successful MAR application, artifact magnitude
- Exp: volume and surface area accuracy, CNR, and sphericity
- Max: CT number accuracy, and segmentation algorithm improvement suggestions

MAR algorithm:
- Min: successful MAR application
- Exp: mentioned above
- Max: none

Unfortunately, surgical clips used in neurovascular aneurysm clipping were not obtained. The second experimental stage procedure was not completed; only data for a partially coil-filled aneurysm was obtained. Therefore, a fourth experimental stage was planned to obtain data for a fully-coiled aneurysm. The original plan involved acquisition of CT images in both the experimental imaging bench available in the ISTAR lab, and the Zeego in the Interventional Neuroradiology (INR) suite. The plan also involved writing an algorithm that would transfer data between the two CT systems. However, the MAR algorithm made available by the manufacturer could only be used and applied in a dedicated workstation, and could only be applied to data acquired from the Zeego system. This rendered the plan to acquire images on the experimental bench and write a conversion algorithm useless.Finally, the maximum deliverable in the MAR algorithm section was to implement changes in the algorithm. This was unachievable because the algorithm was never made available to the public.

Unexpected dependencies
- Tungsten metal sphere detached from deployment device.
- C-Arm Cone-Beam system was uncalibrated for the first experimental stage image acquisition, which generated geometric calibration artifacts, delaying the MAR application and data analysis progress.
- The MAR prototype needed to be installed in the INR suite, which delayed the progress further.
- A limited number of coils available in the second experimental stage hindered fully-coiling the aneurysm.
- Ideal Onyx system did not work, a secondary system was used instead.
- No clips were available for phantom construction.
- Surgeon schedule was very hectic.

5.2 Division of Tasks

Carolina Cay-Martinez: in charge of project management and project write-ups
Marta Wells: in charge of MATLAB coding for data analysis metrics
Project members were equally involved in phantom construction and image acquisition.

5.4 What was learned

Image visualization is vital in CT-guided interventions. Quantyfying image quality is important for: evaluating new imaging technologies and algorithms, evidence for translation to clinical use and avoiding pitfalls of subjective interpretations.

6. Resources

We would like to give a very special acknowledgment to Adam S. Wang for his extraordinary help in the phantom construction and image acquisition. We would also like to acknowledge Rohkohl and B. Scholz for their work in the manufactured MAR algorithm.

[1] Barrett, J. F., and N. Keat. "Artifacts in CT: Recognition and Avoidance." Radiographics 24.6 (2004): 1679-691. Print.
[2] Prell, D., Y. Kyriakou, T. Struffert, A. Dorfler, and W. A. Kalender. "Metal Artifact Reduction for Clipping and Coiling in Interventional C-Arm CT." American Journal of Neuroradiology 31.4 (2010): 634-39. Print.
[3] Prell, D., Y. Kyriakou, T. Struffert, M. Beister, and W. A. Kalender. "A novel forward-projection based metal artifact reduction method for flat-detector computed tomography." Physics in Medicine and Biology 54 (2009): 6575-91. Print.
[4] Prince, Jerry L., and Jonathan M. Links. Medical Imaging Signals and Systems. Upper Saddle River, NJ: Pearson Prentice Hall, 2006. Prince.

7. Appendix

A.1 Image acquisition procedure for first stage phantom

Note that the 12.7 mm tungsten sphere unfortunately detached from its plastic rod after its insertion. It could not be recovered and in order to move it out of the region of interest near the clivus it had to be introduced further into the phantom; its final location was in the anterior part of the frontal lobe. The experimental steps and image acquisition up to the 14th image needed to be repeated due to data truncation (loss of information). The field of view was successfully adjusted. Members present in the acquisition were: Jeffrey Siewerdsen, Marty Radvany, Adam Wang, Carolina Cay and Marta Wells. Following is a description of the images taken and notes regarding the process:

Image Number	Metal Components (color coding)	Notes
1	No metal spheres	Control (v.1): 12 plastic spheres in various locations.
2	3.2 mm, steel (small green)	
3	3.2 mm, tungsten (small blue)	
4	3.2 mm, titanium (small red)	
5	6.4 mm, steel (medium green)	
6	6.4 mm, tungsten (medium blue)	
7	6.4 mm, titanium (medium red)	
8	12.7 mm steel (large green)	
9	12.7 mm tungsten (large blue)	Sphere detached from plastic insertion rod, was inserted further into phantom.
10	12.7 mm titanium (large red)	Includes the 12.7 mm tungsten positioned in frontal lobe.
11	No metal spheres	Control (v.2): 12 plastic spheres in various locations and 12.7 mm tungsten in frontal lobe
12	3.2 mm, titanium (small red) & 3.2 mm, steel (small green)	Patient right & patient left, respectively.
13	3.2 mm, steel (small green)	Image acquisition aborted. Data truncation was noted on all previous images. Field of view (FOV0 corrections were made.
14	3.2 mm, steel (small green)	
15	3.2 mm, tungsten (small blue)	
16	3.2 mm, titanium (small red)	
17	6.4 mm, steel (medium green)	
18	No metal spheres	Control (v.2): 12 plastic spheres in various locations 12.7 mm tungsten in frontal lobe.
19	6.4 mm, tungsten (medium blue)	
20	6.4 mm, titanium (medium red)	
21	12.7 mm steel (large green)	
22	12.7 mm titanium (large red)	
23	3.2 mm, titanium (small red) & 3.2 mm, steel (small green)	Patient right & patient left, respectively.
24	3.2 mm, titanium (small red) & 3.2 mm, steel (small green)	3.174 mm, steel (small green) adjusted ~5mm to position both spheres in same plane.
25	3.2 mm, tungsten (small blue) & 3.2 mm, steel (small green)	Patient right & patient left, respectively.
26	3.2 mm, tungsten (small blue) & 3.2 mm, steel (small green)	Adjusted to position both spheres in same plane.
27	3.2 mm, tungsten (small blue) & 3.2 mm, titanium (small red)	Patient right & patient left, respectively. Spheres noted to be slightly out of plane.
28	3.2 mm, tungsten (small blue) & 3.2 mm, titanium (small red)	Adjusted to position both spheres in same plane.
29	3.2 mm, tungsten (small blue) & 3.2 mm, titanium (small red)	Adjusted to position both spheres highly out of plane.

A.2 Image acquisition procedure for second stage phantom

A 4 mm diameter Hemostasis Introducer and an 8 Fr. Introducer sheath were placed in the superior-anterior opening of the phantom to create a seal. The phantom was placed in a prone position, opposite of the normal patient L-R orientation. Tubing of inferior-posterior opening was kept clamped and out of the FOV during procedures. A volume of 180 mL proved to be enough to displace the solution inside the phantom. Equipment was flushed with the solution inside the phantom previous to introduction to ensure non-dilution. Components used in this phantom coiling procedure include: 0.36mm diameter Neuro Guide Wire (Boston Scientific), 0.75 mm diameter infusion catheter (Johnson & Johnson), 4.50 mm diameter stent (Enterprise, DePuy), 12mmx42cm Resistant Coil (DePuy), 8mmx20cm Resistant Coil (DePuy), and 7mmx16cm Resistant Coil (DePuy).

Note that the first stent deployment was unsuccessful due to the incompatibility in size between the selected stent delivery system and the infusion catheter. A larger catheter was substituted in its place and a new stent system was successfully deployed. The iodine contrast solution was heated in order to activate the stent deployment. Additionally, although 3 coils were successfully introduced, the aneurysm was not fully

Image Number	Components	Notes
1	Non-contrast distilled water in vessel	Control Image
2	30mgI/mL iodine contrast in vessel	
3	30mgI/mL iodine contrast in vessel, 0.36mm Neuro Guide Wire	Image used to verify position of wire in relation to aneurysm
4	30mgI/mL iodine contrast in vessel, 0.36mm Neuro Guide Wire, 0.75 mm infusion catheter	Image used to verify position of catheter in relation to aneurysm
5	30mgI/mL iodine contrast in vessel, 0.36mm Neuro Guide Wire, 0.75 mm infusion catheter, 4.50 mm stent	Previous catheter replaced by new 0.95 mm infusion catheter in order to load stent. Image used to verify stent deployment
6	30mgI/mL iodine contrast in vessel, 0.36mm Neuro Guide Wire, 0.75 mm infusion catheter, 4.50 mm stent	
7	Non-contrast water in vessel, 0.36mm Neuro Guide Wire, 0.75 mm infusion catheter, 4.50 mm stent	
8	30mgI/mL iodine contrast in vessel, 0.36mm Neuro Guide Wire, 0.75 mm infusion catheter, 4.50 mm stent, 18 Stretch Resistant Coil (12mmx42cm)	
9	30mgI/mL iodine contrast in vessel, 0.36mm Neuro Guide Wire, 0.75 mm infusion catheter, 4.50 mm stent, 18 Stretch Resistant Coil (12mmx42cm), 14 Stretch Resistant Coil (8mmx20cm), 10 Stretch Resistant Coil (7mmx16cm)	
10	Non-contrast water in vessel, 0.36mm Neuro Guide Wire, 0.75 mm infusion catheter, 4.50 mm stent, 18 Stretch Resistant Coil (12mmx42cm), 14 Stretch Resistant Coil (8mmx20cm), 10 Stretch Resistant Coil (7mmx16cm)	
11	Non-contrast water in vessel, 18 Stretch Resistant Coil (12mmx42cm), 14 Stretch Resistant Coil (8mmx20cm), 10 Stretch Resistant Coil (7mmx16cm)	Stent, wire and catheter removed
12	30mgI/mL iodine contrast in vessel, 18 Stretch Resistant Coil (12mmx42cm), 14 Stretch Resistant Coil (8mmx20cm), 10 Stretch Resistant Coil (7mmx16cm)	

coiled. Clinician estimates that approximately 50% of the aneurysm volume was successfully coiled. Members present in the acquisition were: Marty Radvany, Adam Wang, Michal Obrzut, Carolina Cay and Marta Wells. Following is a description of the images taken and notes regarding the process:

A.3 Image acquisition procedure for third stage phantom

The Insertion of guide wire and deployment of stent were successful. The iodine contrast solution was heated in order to activate the stent deployment. A hyper form single lumen balloon and the occlusion balloon catheter were inserted. However, they were not successfully threaded through the stent, and were removed. A solution of Onyx 34 MTI was introduced through the specialized catheter directly into the aneurysm. Since the balloon was not inserted successfully, the Onyx leaked out of the aneurysm into the vessel model. Air bubbles were also introduced along with the Onyx solution. Members present in the acquisition were: Marty Radvany, Adam Wang, Michal Obrzut, Carolina Cay and Marta Wells. Following is a description of the images taken and notes regarding the process:

Image Number	Components	Notes
1	Non-contrast distilled water in vessel	Control
2	30mgI/mL iodine contrast in vessel	Control
3	30mgI/mL iodine contrast in vessel, DMSO compatible catheter	
4	30mgI/mL iodine contrast in vessel, DMSO compatible catheter, 4.50 mm stent	
8	30mgI/mL iodine contrast in vessel, DMSO compatible catheter, 4.50 mm stent, Hyper form single lumen balloon, Occlusion balloon catheter	Balloon deployment was unsuccessful
9	30mgI/mL iodine contrast in vessel, DMSO compatible catheter, 4.50 mm stent	DMSO compatible catheter adjusted after slight displacement
10	30mgI/mL iodine contrast in vessel, DMSO compatible catheter, 4.50 mm stent, Onyx 34 MTI	Aneurysm filling incomplete
12	30mgI/mL iodine contrast in vessel, DMSO compatible catheter, 4.50 mm stent, Onyx 34 MTI	
14	Non-contrast distilled water in vessel, DMSO compatible catheter, 4.50 mm stent, Onyx 34 MTI	

A.4 Image acquisition procedure for fourth stage phantom

Members present in the acquisition were: Marty Radvany, Adam Wang, J. Webster Stayman, Carolina Cay and Marta Wells. Following is a description of the images taken and notes regarding the process:

Image Number	Components	Notes
1	Non-contrast distilled water in vessel	Control Image
2	30mgI/mL iodine contrast in vessel	
3	30mgI/mL iodine contrast in vessel, 0.36mm Neuro Guide Wire , 0.75 mm infusion catheter, 4.50 mm stent	Image used to check stent deployment
4	30mgI/mL iodine contrast in vessel, 0.36mm Neuro Guide Wire , 0.75 mm infusion catheter, 4.50 mm stent	Image used to check stent deployment
5	30mgI/mL iodine contrast in vessel, 0.36mm Neuro Guide Wire , 0.75 mm infusion catheter, 4.50 mm stent Penumbra Coil 15mm x 57 cm	
6	30mgI/mL iodine contrast in vessel, 0.36mm Neuro Guide Wire , 0.75 mm infusion catheter, 4.50 mm stent Penumbra Coil 15mm x 57 cm Penumbra Coil 9mm x 60 cm	
7	Noncontrast water in vessel, 0.36mm Neuro Guide Wire , 0.75 mm infusion catheter, 4.50 mm stent Penumbra Coil 15mm x 57 cm Penumbra Coil 9mm x 60 cm	
8	Noncontrast water in vessel, 0.36mm Neuro Guide Wire , 0.75 mm infusion catheter, 4.50 mm stent Penumbra Coil 15mm x 57 cm Penumbra Coil 9mm x 60 cm Penumbra Coil 9 mm x 25 cm Penumbra Coil 7 mm x 15 cm Penumbra Coil 5 mm x 9 cm Penumbra Coil 3 mm x 5 cm Penumbra Coil 2 mm x 4 cm	
9	30mgI/mL iodine contrast in vessel, 0.36mm Neuro Guide Wire , 0.75 mm infusion catheter, 4.50 mm stent Penumbra Coil 15mm x 57 cm Penumbra Coil 9mm x 60 cm Penumbra Coil 9 mm x 25 cm Penumbra Coil 7 mm x 15 cm Penumbra Coil 5 mm x 9 cm Penumbra Coil 3 mm x 5 cm Penumbra Coil 2 mm x 4 cm	

B.1 Data analysis for first experimental stage phantom: metal spheres

Artifact magnitude measurements:

- For the 3.2 mm metal spheres, the center point coordinates of the sphere were located in the image.
    - A rectangular box ROI of 5x5x4 voxels was selected around this center point to represent the area of the sphere.
    - For the background ROI, an area enclosed by the region between two concentric circles (inner radii of 10 voxels and outer radii of 30 voxels) around the center point was selected for each sphere. The background ROI is defined as the left half of this combined region in the four z-planes of interest forming a semicircular annulus.
- For the 6.4 mm metal spheres, the center point coordinates of the sphere were located in the image.
    - A rectangular box ROI of 9x9x8 voxels was selected around this center point to represent the sphere area.
    - For the background ROI, an area enclosed by the region between two concentric circles (inner radii of 16 voxels and outer radii of 34 voxels) around the center point was selected for each sphere. The background ROI is defined as the left half of this combined region in the four z-planes of interest forming a semicircular annulus.
- For the 12.8 mm metal spheres, the center point coordinates of the sphere were located in the image.
    - A rectangular box ROI of 15x15x16 voxels was selected around this center point to represent the sphere area.
    - For the background ROI, an area enclosed by the region between two concentric circles (inner radii of 25 voxels and outer radii of 38 voxels) around the center point was selected for each sphere. The background ROI is defined as the left half of this combined region in the four z-planes of interest forming a semicircular annulus.
    - Note: The 12.8mm tungsten sphere had detached from its insertion rod earlier in the procedure, so we were unable to image it near the clivus, as with the other spheres.
- Quantitative measurements obtained included the mean (μ_{sphere} and $\mu_{background}$), and standard deviation (σ_{sphere} and $\sigma_{background}$) of the attenuation in both the original CT reconstruction images and the corresponding MAR corrected images for each ROI, both sphere and background regions.

Note: The distance between the inner circle of the background ROI and the surface boundary of the spheres was kept constant for each sphere diameter. The area, or number of voxels, within the background ROIs was also kept constant throughout all the sphere diameters. The area measured 1446±12. The distance measured 10 voxels. These selections ensure the reliability of the *artifact magnitude* measurement between the spheres of different diameters.

Segmentation accuracy measurements:
- For the 3.2mm spheres, a circular area of radius 10 voxels around the center of the sphere was selected. The number of voxels within this area that exceeded the threshold level of 5000 HU was counted, and the process was repeated for every z-plane in which the metal sphere was visible in the image. The total number of voxels exceeding the threshold level was summed, and multiplied by the volume of one voxel (0.5x0.5x0.5 = 0.125 mm^3) to obtain the volume estimate of each sphere.
- For the 6.4mm spheres, a circular area of radius 13 voxels around the center of the sphere was selected. The number of voxels within this area that exceeded the threshold level of 5000 HU was counted, and the process was repeated for every z-plane in which the metal sphere was visible in the image. The total number of voxels exceeding the threshold level was summed, and multiplied by the volume of one voxel (0.5x0.5x0.5 = 0.125 mm^3) to obtain the volume estimate of each sphere.
- For the 12.8mm spheres, a circular area of radius 20 voxels around the center of the sphere was selected. The number of voxels within this area that exceeded the threshold level of 5000 HU was counted, and the process was repeated for every z-plane in which the metal sphere was visible in the image. The total number of voxels exceeding the threshold level was summed, and multiplied by the volume of one voxel (0.5x0.5x0.5 = 0.125 mm^3) to obtain the volume estimate of each sphere.
- The surface area for each sphere was calculated through a convolution of the binarized volume matrix to count the exposed faces on each voxel.

- The sphericity of each sphere was calculated as $\psi = \dfrac{\pi^{1/3}(6V_p)^{2/3}}{A_p}$, V_p is the volume and A_p is the surface area of the spheres.

B.2 Data analysis for second and fourth experimental stage phantoms: coils and stent

Artifact magnitude measurements:
- For each image from the second experimental stage phantom that included a significant metal component (the NC and CE vessels with three coils and with and without stent) the center point of the packed coils was measured.
  - A rectangular box ROI of 9x9x8 voxels was selected around this center point to represent the area of the metal component.
  - For the background ROI, an area enclosed by the region between two concentric circles (inner radii of 21 voxels and outer radii of 43 voxels) around the center point was selected for each sphere. The background ROI is defined as the lower left quarter of this combined region, vertically from the lower edge of the outer ring to 15 voxels above the center point, in the eight z-planes of interest forming a semicircular annulus.
- For each image from the fourth experimental stage phantom that included a significant metal component (the NC and CE vessels half- and fully-coiled with stents) the center point of the packed coils was measured.
  - A rectangular box ROI of 9x9x15 voxels was selected around this center point to represent the area of the metal component.
  - For the background ROI, an area enclosed by the region between two concentric circles (inner radii of 35 voxels and outer radii of 56 voxels) around the center point was selected for each sphere. The background ROI is defined as the lower right quarter of this combined region, vertically from the lower edge of the outer ring to the center point, in the fifteen z-planes of interest forming a semicircular annulus.
- Quantitative measurements obtained included the mean (μ_{sphere} and $\mu_{background}$), and standard deviation (σ_{sphere} and $\sigma_{background}$) of the attenuation in both the original CT reconstruction images and the corresponding MAR corrected images for each ROI, both sphere and background regions.

Image fidelity measurements:
- For each image from the second experimental stage phantom that included a significant metal component (the NC and CE vessels with three coils and with and without stent) the center point of the acrylic sphere and polypropylene rod closest to the aneurysm was located.
  - A rectangular box ROI of 11x11x10 voxels was selected around this center point to represent the area of the plastic component.
  - For the background ROI, an area enclosed by the region between two concentric circles (inner radii of 20 voxels and outer radii of 55 voxels) around the center point was selected for each sphere. The background ROI is defined as the right half of this combined region, vertically from 20 voxels below the center point to 20 voxels above the center point, in the ten z-planes of interest forming a semicircular annulus.
- For each image from the fourth experimental stage phantom that included a significant metal component (the NC and CE vessels full-coiled with a stent) the center point of the acrylic sphere and polypropylene rod closest to the aneurysm was located.
  - A rectangular box ROI of 11x11x8 voxels was selected around this center point to represent the area of the plastic component.
  - For the background ROI, an area enclosed by the region between two concentric circles (inner radii of 20 voxels and outer radii of 55 voxels) around the center point was selected for each sphere. The background ROI is defined as the right half of this combined region, vertically from 20 voxels below the center point to 20 voxels above the center point, in the ten z-planes of interest forming a semicircular annulus.

B.3 Data analysis for third stage phantom: liquid embolus and stent

Artifact magnitude measurements:

- For each image from the third experimental stage phantom that included a significant metal component (the NC and CE vessels with Onyx) the center point of the aneurysm was measured.
  - For the background ROI, an area enclosed by the region between two concentric circles (inner radii of 14 voxels and outer radii of 26 voxels) around the center point was selected for each sphere. The background ROI is defined as the left half of this combined region in the ten z-planes of interest forming a semicircular annulus.
- Quantitative measurements obtained include the standard deviation ($\sigma_{background}$) of the attenuation in both the original CT reconstruction images and the corresponding MAR corrected images for the background ROI.

Image fidelity measurements:

- For each image from the third experimental stage phantom that included a significant metal component (the NC and CE vessels with Onyx) the center point of the acrylic sphere and polypropylene rod closest to the aneurysm was located.
  - A rectangular box ROI of 11x11x5 voxels was selected around this center point to represent the area of the plastic component.
  - For the background ROI, an area enclosed by the region between two concentric circles (inner radii of 25 voxels and outer radii of 60 voxels) around the center point was selected for each sphere.
  - The background ROI for the acrylic sphere is defined as the lower half of this combined region, horizontally from 25 voxels left of the center point to 25 voxels right of the center point, in the five z-planes of interest forming a semicircular annulus.
  - The background ROI for the polypropylene rod is defined as the right half of this combined region, vertically from 25 voxels below the center point to 25 voxels above the center point, in the five z-planes of interest forming a semicircular annulus.
- Quantitative measurements obtained include the CNR of each plastic insert, defined as $\frac{\mu_{component} - \mu_{background}}{\sigma_{background}}$, and the percent error in CT number, defined as $\left| \frac{\mu_c^{true} - \mu_c^{measured}}{\mu_c^{true}} \right| \cdot 100$ in both the original CT reconstruction images and the corresponding MAR corrected images.